



OPEN

Tissue heterogeneity in structure and conductivity contribute to cell survival during irreversible electroporation ablation by “electric field sinks”

SUBJECT AREAS:

BIOMEDICAL
ENGINEERING

TRANSLATIONAL RESEARCH

Received
25 July 2014Accepted
7 January 2015Published
16 February 2015Alexander Golberg^{1,2}, Bote G. Bruinsma¹, Basak E. Uygun¹ & Martin L. Yarmush^{1,3}

¹Center for Engineering in Medicine, Department of Surgery, Massachusetts General Hospital, Harvard Medical School, and the Shriners Burns Hospital, Boston, MA 02114, ²Porter School of Environmental Studies, Tel Aviv University, Israel, 6997801, ³Department of Biomedical Engineering, Rutgers University, Piscataway, NJ 08854.

Correspondence and requests for materials should be addressed to M.L.Y. (ireis@sbi.org)

Irreversible electroporation (IRE) is an emerging, minimally invasive technique for solid tumors ablation, under clinical investigation for cancer therapy. IRE affects only the cell membrane, killing cells while preserving the extracellular matrix structure. Current reports indicate tumors recurrence rate after IRE averaging 31% of the cases, of which 10% are local recurrences. The mechanisms for these recurrences are not known and new explanations for incomplete cell death are needed. Using finite elements method for electric field distribution, we show that presence of vascular structures with blood leads to the redistribution of electric fields leading to the areas with more than 60% reduced electric field strength in proximity to large blood vessels and clustered vessel structures. In an *in vivo* rat model of liver IRE ablation, we show that cells located in the proximity of larger vessel structures and in proximity of clustered vessel structures appear less affected by IRE ablation than cells in the tissue parenchyma or in the proximity of small, more isolated vessels. These findings suggest a role for “electric field sinks” in local tumors recurrences after IRE and emphasize the importance of the precise mapping of the targeted organ structure and conductivity for planning of electroporation procedures.

Electroporation is a minimally invasive technique that uses externally-applied pulsed electric fields to increase cell membrane permeability¹. In the case of reversible electroporation, cell membrane permeabilization is temporary and the treated cells survive², while irreversible electroporation (IRE) is application of pulsed electric fields above a certain threshold after which the cells die post treatment^{2,3}. Reversible electroporation is currently used for clinical procedures known as electrochemotherapy and gene electro transfer². IRE applications originate in the early 1960s, when it was applied for non-thermal food sterilization and plant tissue decomposition^{4–8}. Over the last decade the application of IRE expanded to the medical field; solid tumor ablation, drug sterilization and recently to hemostasis and disinfection of wounds^{9–15}.

IRE has emerged as a non-thermal alternative to tissue ablation methods such as cryosurgery and radiofrequency ablation (RFA) for the treatment of solid tumors. Promising results from pre-clinical studies in cell culture¹⁶ and small and large animal models^{17,18} led to the FDA 510 k clearance in 2006 for the soft tissue ablation. Several groups conducting clinical trials demonstrated the safety profile of IRE in the clinical setting^{19,20}. At the time of writing, there are 14 registered clinical trials, 5 of which are actively recruiting patients, which aim to evaluate the efficacy of IRE on the ablation of solid tumors²¹.

Initial results from the first clinical applications show a large distribution of tumor recurrence rates, ranging from 5–100% between trials^{3,19,22–25}, and the complete response rate ranged from 0 to 100%, depending on the tissue type^{19,23}. Most of the experience with IRE ablation is in the treatment of pancreas and liver tumors. In a recent review of a multi-institutional prospectively-collected registry of 150 patients undergoing 169 IRE ablations from 2009 through 2012, 31% of the patients had recurrence in the median follow up of 18 months¹⁹. Of the total 31%, 10.7% were local recurrences at the ablated site¹⁹. The authors suggested a trend of increased recurrences with larger lesions, lesions involving vascular invasion and pancreatic lesions¹⁹. In comparison, the most recently reported recurrence rates for RFA and percutaneous ethanol injection are approximately 2–15% and 11–35% after 2 years, respectively²⁶.



In the view of the ongoing clinical trials and high recurrence rates of the IRE ablated tumors, there is an urgent need to reveal the mechanisms behind tumor recurrence to improve the clinical efficacy of IRE. The goal of this study was to test the hypothesis that heterogeneity in organ structure and electrical conductivity, predicated by the chemical composition, affect the efficacy of IRE in ablating cells. Although the exact mechanisms of cell death after exposure to IRE are not completely understood, a large body of evidence from both cell culture and animal studies shows that cells should be exposed to an electric field strength larger than an IRE threshold field value, for the successful application of IRE^{17,27}.

The liver was chosen in this work to exemplify heterogeneity in an organ microstructure and chemical composition as it is a highly vascularized organ. In electroporation procedures modeling, the liver is often considered a homogeneous parenchymal tissue with uniform conductivity, but the parenchymal tissue is permeated by a hierarchical network of branching blood and biliary vessels that become systematically smaller away from the hepatic hilum, where the inflow vessels enter and the bile duct exits the organ. The branches of portal vein, hepatic artery and bile ducts run in parallel and in a clustered distribution, forming a triad of vessels that show similarity at various scales.

Using numerical modeling and *in vivo* IRE ablation of the rat liver and, we examine the effects of intrahepatic structures, such as blood vessels, their size and their clustering, on the electric field distributions around the vessel wall and adjacent tissue survival.

Methods

All experiments were performed in accordance with relevant guidelines and regulations.

Numerical simulations. To model the distribution of the electric fields in the liver and its compartments, we used the finite elements method (FEM), which allows us to find an approximate solution in complex geometries for Laplace differentiation equation with boundary conditions defined by the applied voltage. Numerical solutions for a Laplace equation that result in the electric field distribution in the liver model were performed in QuickField (Terra Analysis, Denmark).

Animal subjects. Female Lewis rats (180–250 g, 6-weeks old) were obtained from Charles River Laboratories (Wilmington, MA). The animals were housed in individual cages with access to food and water ad libitum, and were maintained on a 12-hour light/dark cycle in a temperature controlled room. All animal procedures were approved by the Institutional Animal Care and Use Committee (IACUC) of the Massachusetts General Hospital and were kept in accordance with the guidelines of the National Research Council.

***In vivo* liver electroporation.** Twenty minutes prior to induction of anesthesia, 0.05 mg/kg of buprenorphine was administered subcutaneously. Rats were anesthetized by inhalation of isoflurane (5% in oxygen) in an Ohmeda Tech 4 tabletop anesthesia apparatus connected to a standard rodent system. The animal was placed in a supine position on a sterile surgical table. The abdomen was opened with a

25 mm midline incision from the xyphoid process down and the sternum and abdominal wall were retracted. Two non-thermal IRE ablations were performed on different lobes using small, 7 mm (diameter) BTX Tweezerrodes (Harvard apparatus, MA), which reduced the concentration of the current on electrodes tips, rapid drops in the electric fields and edge thermal effects associated with the needle electrodes. The electroporation protocols used in this study was as follows: electrode separation: 3 mm, applied voltages: 120 V, 240 V, 360 V, 480 V, 600 V, 720 V number of pulses: 99, pulse length 50 μ s, frequency of pulse delivery: 4 Hz. Square pulses were delivered using BTX 830 pulse generator (Harvard Apparatus Inc, Holliston MA, USA). Currents were measured *in vivo* using PicoScope 4224 Oscilloscope with Pico Current Clamp (60A AC/DC) and analyzed with Pico Scope 6 software (Pico technologies Inc., UK). The abdomen was irrigated with 0.9% saline solution and the wound was closed in two layers using 4–0 silk sutures.

Histology. Tissue specimens were harvested 24 hours (360 V, $n = 3$) and 72 hours (120 V, 240 V, 360 V, 480 V, 600 V, 720 V, $n = 3$ per voltage) following the initial IRE ablation. Liver samples were fixed in 10% formalin, embedded in paraffin, and cut into 5 μ m sections. Sections were stained with hematoxylin and eosin (H&E) stain. Tissue was processed and stained by the Rodent Histopathology Core at Harvard Medical School. Slides were evaluated by three separate investigators. Color images of each entire tissue section were acquired using NanoZoomer Digital Pathology System (Nanozoomer 2.0-HT slide scanner (Hamamatsu, Hamamatsu City, Japan)).

Immunohistochemical staining. Paraffin-embedded tissue sections (5 μ m) on glass slides were baked at 60 °C for 30 minutes, followed by deparaffinization in xylene and rehydration in graded alcohol into water. Antigen retrieval was performed by boiling the slides in 10 mM Sodium Citrate buffer pH = 6.0 for 30 minutes. Endogenous peroxidase activity was quenched with Dual Endogenous Enzyme Block (DAKO, Denmark) for 5 minutes. Tissue sections were incubated with 1 : 100 dilution of Ki67 rabbit monoclonal antibody (Abcam, Cambridge MA, 16667) in 1% TBS/BSA at room temperature inside a humidified chamber for 30 minutes. After washing, slides were incubated with Rabbit Polymer (DAKO, Denmark) reagent for 30 min at RT followed by incubation with the DAB+ reagent (DAKO, Denmark) with monitoring for 5–10 minutes. After washing, counterstain was done using Harris type Hematoxylin. Slides were briefly dehydrated and then mounted with Histomount solution (Life Technologies, Grand Island, NY 008030). Color images of each entire tissue section were acquired using NanoZoomer Digital Pathology System (Nanozoomer 2.0-HT slide scanner, Hamamatsu, Hamamatsu City, Japan). The number of cells that are positive for Ki67 was counted using the software ImageJ (NIH, MA). The statistical significance of the difference in results was analyzed using Student's t-test.

Results

Liver heterogeneity affects electric field distribution. As mentioned previously, the efficacy of electroporation on the single cell level is dependent on the local electric field strength that the cell is exposed to. In order to identify whether a possible non-uniform cell death observed within the liver tissue is a result of uneven electric field distribution, we performed numerical simulations of the electric field generated by IRE treatment. Fig. 1a shows the model geometry used in this study where the target liver region, the externally positioned electrodes and the surrounding air are depicted. The liver was modeled as homogeneous parenchymal tissue with vascular structures. The vessel diameters were set as 50, 100 and

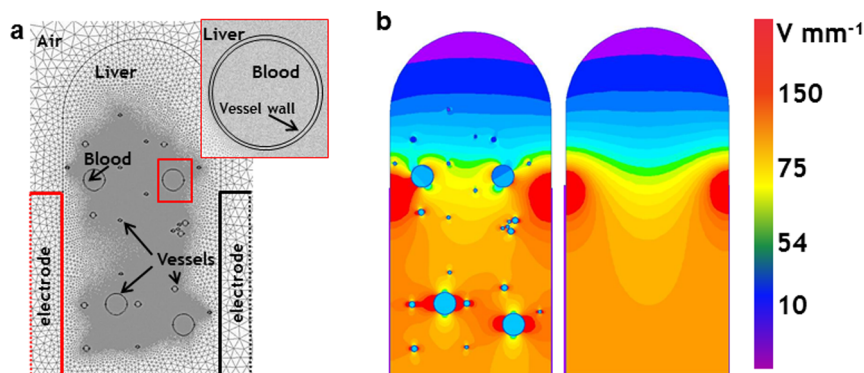


Figure 1 | The impact of liver heterogeneity in structure and electrical conductivity on the electric field distribution. (a). Finite elements model of the liver lobe and applied electrodes geometry and structure. We used an axisymmetric model where the major axes is in the center of the lobe (b). Comparison of electric field distribution inside the lobe modeled using a homogeneous organ (right panel) and lobe modeled using an organ with multiple compartments (left panel) when each of the compartments has an individual conductivity.


Table 1 | Electric properties of liver components used in the model

System component	Electrical Conductivity (S m ⁻¹)	Ref
Parenchymal liver (electroporated)	0.13	[34]
Blood	0.7	[34]
Vessel wall	0.17	[35]

200 μm. Each vessel was modeled with a lumen containing blood and external vessel wall (10 μm thickness). Table 1 shows the electrical conductivities used for different liver compartments.

Tissues have both electrical resistance and capacitance properties. However, the charging time of the capacitor component of a healthy liver is very small in comparison to the pulse length^{29,30}. Therefore, we used direct current (DC) conductance model to calculate the distribution of the electric fields in the heterogeneous liver structure. In our model, we used the following Eq. 1 to calculate the local electric field strength in each element of the liver

$$\frac{\partial}{\partial x} \left(\sigma_x(E) \cdot \frac{\partial U}{\partial x} \right) + \frac{\partial}{\partial y} \left(\sigma_y(E) \cdot \frac{\partial U}{\partial y} \right) = 0 \quad (1)$$

where σ is the electrical conductivity (S m⁻¹), and U (V) is the electric potential, E is the local electric field (Vmm⁻¹), and x and y are the direction vectors. The electrical conductivity of the tissue changes due to the exposure to the electric fields. In this work we modeled the electrical conductivity of the parenchymal liver as follows:

$$\sigma = \begin{cases} 0.02, S m^{-1} & E=0 \\ 0.13, S m^{-1} & E \neq 0 \end{cases} \quad (2)$$

We simulated the electric field distribution in different liver compartment layers under the following boundary conditions applied on two electrodes

$$\begin{aligned} U_1 &= 360(V) \\ U_2 &= 0(V) \end{aligned} \quad (3)$$

where U_1 is the potential applied on the cathode and U_2 (0 V) is the potential on the grounded anode.

Structural and conductivity heterogeneity affect the electric field distribution (Fig. 1b). We compared the solution of Eq. 1 between a fully homogeneous liver structure and liver tissue with a heterogeneous structure incorporating vessel structures. The comparison between these two models clearly shows the effect of heterogeneity on electric field distribution, with clearly detectable areas of increased (red) and decreased (green) electric fields or “electric field sinks”, depending on the plane (Fig. 1b, left panel).

Next, we more closely examined the impact of a single vessel filled with blood on the electric field distribution in parenchymal liver tissue. To investigate the effect of single vessels on electric field distributions, we constructed the electric field map (Fig. 2a, left panel) and current density map (Fig. 2a, right panel) in the presence of a blood vessel with a 200 μm diameter. The map shows an increase in the electric field strength in the areas around the vessel in the plane perpendicular to the electrodes (Fig. 2a left panel, red). Oppositely,

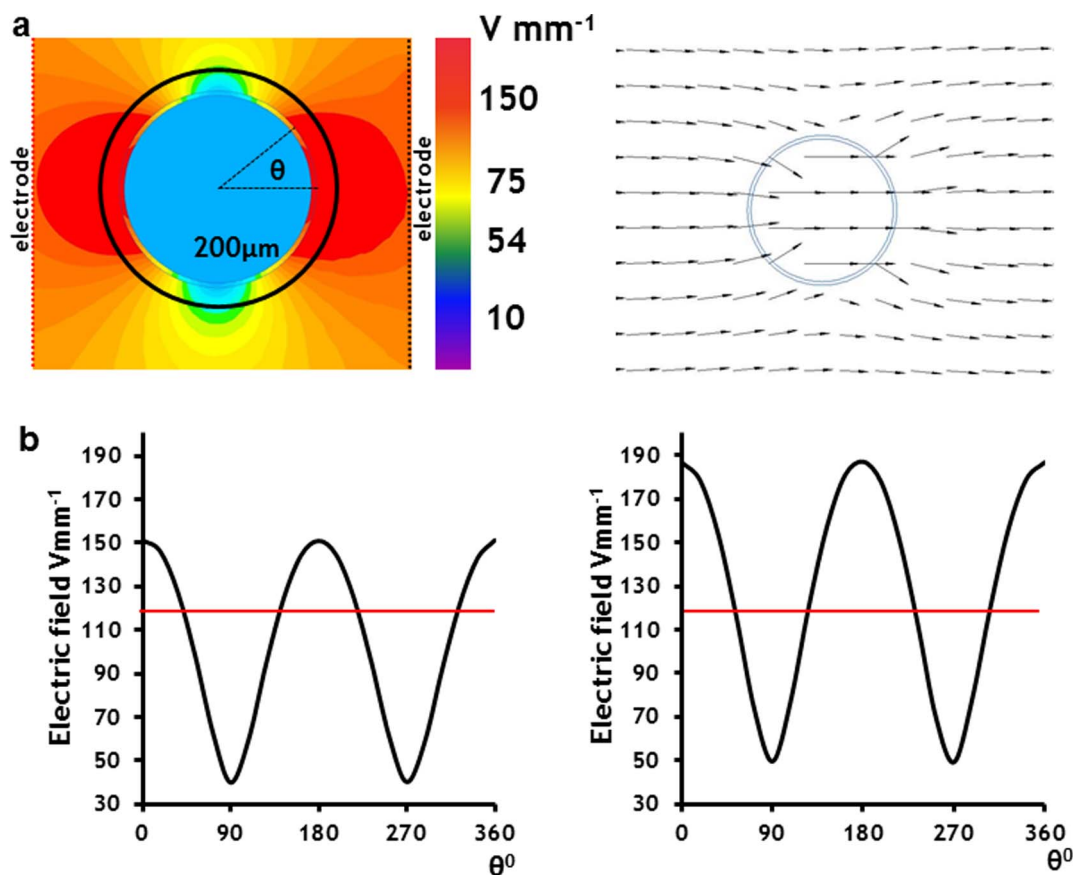


Figure 2 | The effect of a single vessel on the electric field and current distribution. (a). FEM model of electric field distribution (left panel) and current flow (right panel) in and around a single 200-μm vessel that contains blood. (b). Electric field intensity profile in the vessel wall. (c). Electric field intensity profile inside the liver parenchymal tissue at 10 μm distance from the surface of the vessel wall. θ is the angle between the vessel surface vector and the vector of the electric field direction. Red line shows the average intensity of the electric field in liver if the liver is modeled as a homogeneous structure without compartments or the electric field intensity in the areas far away from the areas of heterogeneous conductivity.

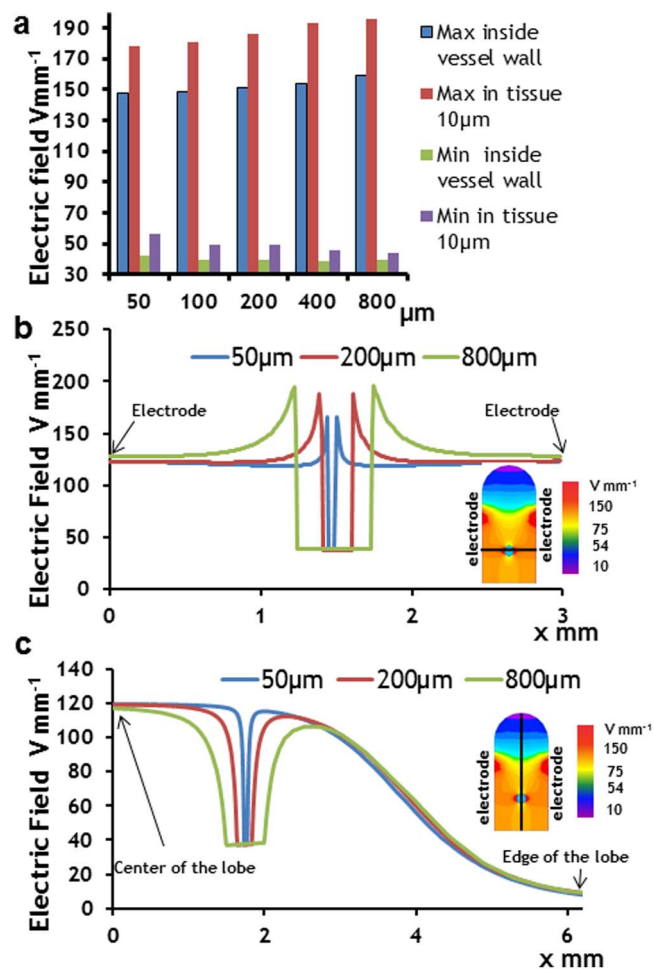


Figure 3 | The impact of the vessel size on the electric field distribution. (a). The impact of the vessel size on the maximum and minimum electric field intensity inside the vessel wall and inside the bulk tissue 10 μm from the vessel. (b). Distribution of electric field intensity along the plane perpendicular to the plane of electrodes (black line on the inset) in proximity and inside the vessels with 50 μm , 200 μm and 800 μm diameter. (c). Distribution of the electric field intensity along the plane parallel to the plane of electrodes (black line on the inset) in proximity and inside the vessels with 50 μm , 200 μm and 800 μm diameter.

the vessel wall and the tissue surrounding the vessel in a plane parallel to the electrodes show a marked decrease in electric field strength (Fig. 2a left panel blue and green). Presence of a highly conductive blood vessel also redirected the electric current – there was more current through high conductive compartment (blood), leading to “current sinks” in the areas of the tissue in planes parallel to the electrodes (Fig. 2a right panel). The electric field distribution inside the blood vessel wall (left panel) and inside the bulk tissue at 10 μm from the vessel (right panel) are shown at Fig. 2b. We chose the distance of 10 μm as this models the exposure of a single bordering parenchymal cell layer to electric field. Survival of such a layer in the case of tumor ablation could lead to the local recurrence. The variations of the local electric fields vary between 40 to 151 Vmm^{-1} within the vessel wall (potentially affecting endothelial cells) and 49 to 186 Vmm^{-1} in the liver parenchyma 10 μm from the vessel. These variations of local electric fields imply that cells residing in those areas will be exposed to different electric fields, potentially lower than the minimum field strength required for complete ablation.

The impact of vessel size on electric field distribution. The impact of the vessel size on the minimum and maximum electric field

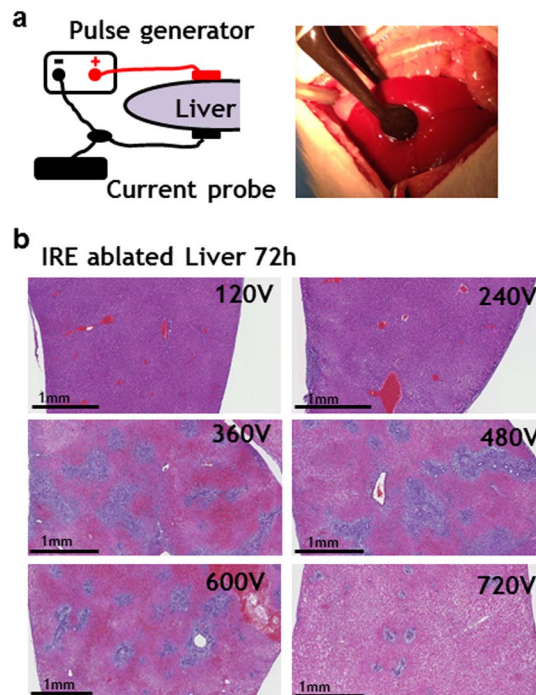


Figure 4 | Rat liver *in vivo* irreversible electroporation dose response. (a). Schematic representation of the experimental system (left panel). Digital photography of electrodes’ position on the liver during pulse delivery. (b). Hematoxylin and eosin stain (H&E) of rat liver tissue treated with 120–720 V and harvested 72 h after ablation.

strengths in the vessel walls and in the liver parenchyma 10 μm from the vessel is shown on Fig. 3a. Increasing the vessel diameter from 50 μm to 800 μm , increased the strength of the electric field in the plane perpendicular to the plane of electrodes by 7.4% inside the vessel wall and by 10.1% in the liver parenchyma. Increasing the vessel diameter from 50 μm to 800 μm , decreased the strength of the electric field in the plane parallel to the plane of electrodes by 4.7% inside the vessel wall and by 21.4% in the liver parenchyma.

The electric field distribution along the plane perpendicular to the electrodes and passing through the center of the blood vessel is shown on Fig. 3b. The electric field distribution along the plane parallel to the electrodes and passing through the center of the blood vessel, located in the center of a liver is shown in Fig. 3c. In Fig. 3c one side of the model is a center of the treated liver lobe and the right end is the edge of the lobe. Therefore, the electric field distribution is asymmetric. In comparison with the average electric field in the homogeneous liver (120 Vmm^{-1}), vessels with 800 μm diameter increased the strength of the electric field in the plane perpendicular to the plane of electrodes by 32.5% inside the vessel wall and by 63.3% in the liver parenchyma, and decreased the strength of the electric field in the plane parallel to the plane of electrodes by 66.6% inside the vessel wall and by 63.3% in the liver parenchyma.

Irreversible electroporation of rat liver *in vivo*- dose response studies. Liver ablation was performed *in vivo* using a set of parallel round electrodes. We chose to work with this system to avoid current concentration on electrodes tips, rapid drops in the electric fields and edge thermal effects associated with the needle electrodes. The schematic design and a representative actual image of the *in vivo* electrode set-up are shown in Fig. 4a left panel.

The electroporation protocol (120 V, 240 V, 360 V, 480 V, 600 V, 720 V number of pulses: 99, pulse length 50 μs , frequency of pulse delivery: 4 Hz) was delivered to each rat liver. Tissue was harvested seventy-two hours after ablation to observe the maximum

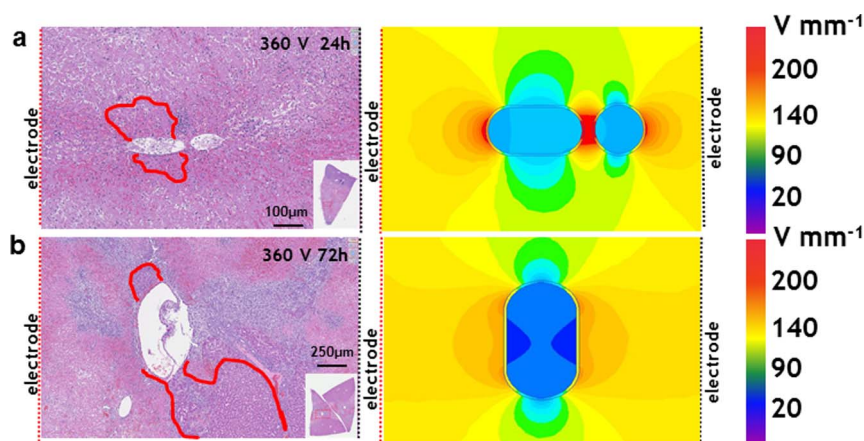


Figure 5 | Electric field sinks after IRE ablation *in vivo*. (a). Reconstruction of an area of the liver with multiple tubular structures. Left image shows a histological area of a treated liver lobe (H&E stain) 24 hours after ablation. Right image shows the respective corroborating FEM model of electric field distribution in the area. (b). Reconstruction of an area of the liver with a single large vessel of a treated liver lobe (H&E stain) 72 hours after ablation. (left panel). The corresponding reconstructed FEM modeling of predicted electric field distribution in the area (right panel). Red demarcation shows live hepatocytes determined by H&E in the areas of electric field sinks. Color scale bars on left show the color map for the electric field intensity.

ablation effects: maximum ablation with not yet significantly started regeneration. A clear increase of the damage was observed with increasing of the applied voltage (Fig. 4b). A very sharp transition in the ablation results was observed between 240 V and 360 V. While very few cells were ablated at 240 V, a very dramatic increase in damage was observed at 360 V (Fig. 4b) with the gross pathological observation of massive hepatocyte death.

Vessel clusters and large individual vessels lead to electric fields sinks which support cell survival after IRE *in vivo*. We next examined the effects of liver heterogeneity on cell survival *in vivo*. For these studies we focused on one IRE protocol, in which the applied voltage was the smallest (to reduce the heat effects and the damage to non-target tissue), while leading to a prominent damage as observed in the dose-response experiments. This is also a dosage close to reported in some trials for tumor ablations. The electroporation protocol: 99 pulses at 360 V with pulse duration of 50 μ s at 4 Hz delivered an average current of 0.4 ± 0.02 A. After pulse application, a visual darkening of the treated liver area, which is consistent with the reported red blood cell aggregation due to stasis and vascular lock induced by electroporation based treatments². Twenty-four hours after ablation, the IRE treated liver shows a well-demarcated treatment area on histological examination (Fig. 5a, left insert). Interestingly, cell survival was observed in areas of vessel clustering (Fig. 5a, left, areas with survived cells are demarcated with a red line). To model the electric field distribution in the areas of vessel clustering, we reconstructed the geometry of two liver structures using FEM methods and solved Eq. 1 and 2 for these specific structures (Fig. 5a, right). The resulting distribution of electric fields showed a striking reduction of the electric field intensity in the areas between densely packed vascular structures in the plane parallel to the electrodes. In the plane perpendicular to the electrodes, a striking increase in electric field strength was observed close to the vessel walls corresponding to the areas where cell death is observed.

Our model predicted that large electric field sinks could occur in the poles of the single vessels in the plane parallel to the plane of the electrodes. Correspondingly, hepatocytes located near large blood vessels, in the plane parallel to the electrodes survived a 360 V treatment as long as 72 hours after ablation (Fig. 5b, left, areas with survived cells are demarcated with a red line). To identify the fate of the cells at the area of the vessels, we stained the samples treated by 360 V and harvested 72 hours after ablation for the proliferation marker, Ki67 (Fig. 6a). Not all but some cells in areas close to the

vessels (Area 1) were mitotic (Fig 6b) although significantly less number of cells were Ki67 positive in areas further away from the vessels (Fig 6c). Quantification of number of cells in both areas revealed that areas of the liver parenchyma near the large vascular structures showed two orders of magnitude more cells positive for Ki67 in comparison with distant from large structures areas which showed very low numbers of proliferating cells (Fig. 6d, $P < 0.01$). These findings are consistent with previous work that showed the survival and activation of endothelial and ductal cells after liver IRE ablation²⁸.

Discussion

Non-thermal IRE ablation of tumors is a promising and minimally invasive therapeutic option. However, the reports of high incidences of local recurrences following IRE have been reason for concern and have warranted further investigation. The current rate of local recurrences in pancreatic and hepatic tumors is 10.7%. In this work we have shown that tissue structure and chemical composition, which dictate the electric conductivity, crucially influence the electric field distribution and hence cell survival upon IRE treatment. Combined, our results show that natural heterogeneity in liver structure and electric conductivity create areas of higher or lower electric field strengths than average strengths predicted by a homogenous liver model. Both higher and lower field strengths are relevant for tissue ablation implications. Increased electric fields could lead to the increased temperature due to the treatment and thus destroy the extracellular matrix architecture, preservation of which could be instrumental for reduced post-treatment fibrosis. Importantly, reduced electric fields and “electric fields sinks” could lead to incomplete ablation of malignant cells and thus lead to the local tumors recurrence. Our results show that these effects are more pronounced in areas surrounding larger vascular structures as electric field sinks are larger. Vessel size in the liver ranges from greater than 10 mm at the hepatic portal vein to smaller than 10 μ m at the sinusoidal level and the effects of electric field sinks will be marked if larger vascular structures are involved at the tumor site.

The local electric field strength in tissue is predicated by the area geometry and the conductivity map of the target organ¹⁷. Organs are heterogeneous structures composed of multiple compartments with individual specific conductivities. Previous numerical modeling studies on pulsed electric field distribution in the heterogeneous tissues have shown an increase in the electric field strength in tissues surrounding vessel structures. Increasing the size of the vessels was

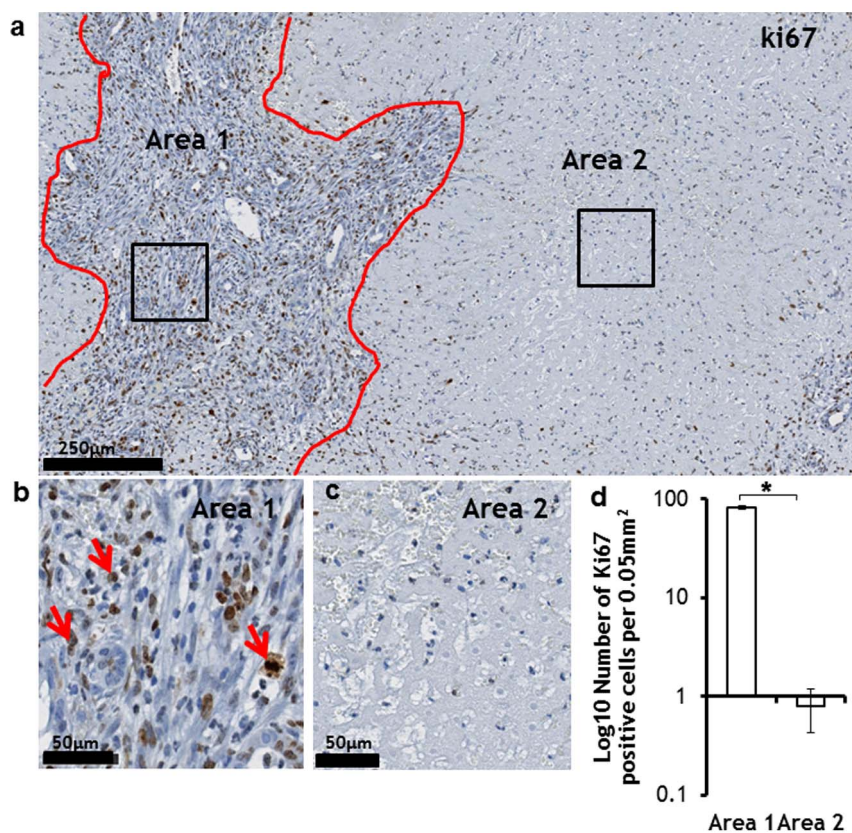


Figure 6 | Cell fate at the IRE ablated areas. (a). Tissue was harvested 72 h after IRE ablation. IHC staining for Ki67 of the liver section treated by 360 V is shown. Demarcated by a black solid line Area 1 is the area in proximity of a large vessel where active proliferation was observed. Red asterisks indicate vessel structures in Area 1. Area 2 shows an ablated area remote from the large vessel and deficient in proliferating cells. (b). Magnification of the black box from Area 2 demonstrating a lack of proliferating cells. (c). Magnification of the black box from Area 1 demonstrating proliferating cells with a red arrow. (d). Ki67 positive cells were quantified by counting in both areas. (* $P < 0.01$). Error bars show the SEM.

shown to increase the electric fields on the endothelial cells facing the electrodes³¹. However, according to the principle of conservation of electric charge, an increase in the electric field strength in certain parts of the tissue must lead to emergence of areas with electric field values lower than the electric field in the homogeneous tissue. These electric field sinks originate inside the blood vessels; however, the transitional zone of the low electric field in the parenchyma is significantly larger and encompasses adjacent cells, protecting from the IRE induced death. Our results show that the existence of electric field sinks is corroborated in both the numerical simulations as well as in vivo, with histological survival patterns both 24 and 72 hours after treatment corroborating models for the relevant tissue. The observed cell survival near large vessels and vascular structures and in the areas of vascular clustering is concerning, as it may lead to the survival of targeted cells surrounding vascular structures during IRE ablation.

In this study we demonstrated the effect of tissue structure and conductivity on the electric fields distributions in the normal liver. Tumors structure and properties can be different and it can be anticipated that angiogenic processes in a tumor produce blood vessels that might have different electric properties than those reported in this study. Moreover, in 2-dimensional liver sections the vasculature represents approximately 2% of the surface in normal liver tissue. Importantly, as a result of stimulated vessel growth in tumorous tissue, the heterogeneity of the tissue increases more than 2-fold to a mean value of nearly 4.5%³², making the heterogeneity of tumorous tissue more pronounced.

Our results are of particular importance to IRE, and other electro-poration based tumor ablation therapies such as electrochemotherapy and gene electro transfer, which also require a complete coverage

of a targeted tissue by electric field higher than a certain threshold². Given these results, we emphasize the importance of a detailed treatment planning process, which could help to reduce the tumor recurrences. An interesting recent work has introduced a method to map liver vasculature for the electroporation process using magnetic resonance imaging (MRI)³³. We suggest that the treatment dose should be determined based on the actual minimal electric field distribution in the compartmented organ, rather than by the average organ conductivity. The full coverage of the tumor can be achieved using multi-electrode system or by rotation of the two-electrode system at different angles. The precise treatment planning will ensure correct electrode positioning and the required applied voltage to cover the whole targeted area with the minimally required electric fields to induce electroporation in the target tissue.

Conclusions

In this work we show in a model of heterogeneous liver structure and conductivity that cell survival near the large vascular structures may result from “electric fields sinks” created in these areas. The depth of the electric field sinks is shown to be dependent on the vessel size and vessel clustering. The cells located in the “electric field sinks” are exposed to less than 40% of the electric field strength average in a homogeneous organ, resulting in survival of hepatocytes in an in vivo rat liver exemplification. These findings imply the importance of precise mapping and post-operational imaging of the targeted organ structure and conductivity for planning of electroporation-based procedures.

1. Neumann, E. *et al.* Gene transfer into mouse lyoma cells by electroporation in high electric fields. *EMBO Journal* **1**, 841–845 (1982).



2. Yarmush, M. L. *et al.* Electroporation-Based Technologies for Medicine: Principles, Applications, and Challenges. *Annu Rev Biomed Eng* **16**, 295–320 (2014).
3. Golberg, A. Y. & Yarmush, M. L. Nonthermal Irreversible Electroporation: Fundamentals, Applications, and Challenges. *IEEE T Biom Eng* **60**, 707–714 (2013).
4. Zagorulko, A. J. [Technological parameters of beet desugaring process by the selective electropolymolysis]. *New physical methods of foods processing*, [21–27] (Izdatelstvo GosINTI, Moscow, 1958).
5. Doevenspeck, H. Influencing cells and cell walls by electrostatic impulses. *Fleishwirtschaft* **13**, 986–987 (1961).
6. Hamilton, W. A. & Sale, A. J. Effect of high electric field on micro-organisms. II. Mechanism of action of the lethal effect. *Biochim Biophys Acta* **148**, 788–800 (1967).
7. Sale, A. J. & Hamilton, W. A. Effect of high electric field on micro-organisms. I. Killing of bacteria and yeast. *Biochim Biophys Acta* **148**, 781–788 (1967).
8. Sale, A. J. & Hamilton, W. A. Effects of high electric fields on microorganisms. III. Lysis of erythrocytes and protoplasts. *Biochim Biophys* **163**, 37–43 (1968).
9. Davalos, R., Mir, L. M. & Rubinsky, B. Tissue Ablation with Irreversible Electroporation. *Ann Biomed Eng* **33**, 223–231 (2005).
10. Rubinsky, B., Onik, G. & Mikus, P. Irreversible Electroporation: A New Ablation Modality – Clinical Implications. *Technol Cancer Res Treat* **6**, 37–48 (2007).
11. Golberg, A., Belkin, M. & Rubinsky, B. Irreversible electroporation for microbial control of drugs in solution. *AAPS PharmSciTech* **10**, 881–6 (2009).
12. Gusbeth, C. *et al.* Pulsed electric field treatment for bacteria reduction and its impact on hospital wastewater. *Chemosphere* **75**, 228–33 (2009).
13. Golberg, A. *et al.* Non-Thermal, Pulsed Electric Field Cell Ablation: A Novel Tool for Regenerative Medicine and Scarless Skin Regeneration. *Technology* **1**, 1–8 (2013).
14. Mandel, Y. *et al.* Hemorrhage Control of Liver Injury by Short Electrical Pulses. *PLoS ONE* **8**, e49852 (2013).
15. Golberg, A. *et al.* Eradication of multidrug-resistant *A. baumannii* in burn wounds by antiseptic pulsed electric field. *Technology* **2**, 1–8 (2014).
16. Miller, L., Leor, J. & Rubinsky, B. Cancer cells ablation with irreversible electroporation. *Technol Cancer Res Treat* **4**, 699–705 (2005).
17. Rubinsky, B. *Irreversible Electroporation* (Springer, 2010).
18. Rubinsky, B., Onik, G. & Mikus, P. Irreversible Electroporation: A New Ablation Modality – Clinical Implications. *Technol Cancer Res Treat* **6**, 37–48 (2007).
19. Philips, P., Hays, D. & Martin, R. C. Irreversible electroporation ablation (IRE) of unresectable soft tissue tumors: learning curve evaluation in the first 150 patients treated. *PLoS One* **8**, e76260 (2013).
20. Thomson, K. R. *et al.* Investigation of the safety of irreversible electroporation in humans. *J Vasc Interv Radiol* **22**, 611–21 (2011).
21. Clinical Trials Registry, A service of National Institute of Health <http://clinicaltrials.gov/> (accessed: 14 July 2014).
22. Kingham, T. P. *et al.* Ablation of perivascular hepatic malignant tumors with irreversible electroporation. *J Am Coll Surg* **215**, 379–87 (2012).
23. Usman, M. *et al.* Irreversible electroporation of lung neoplasm: a case series. *Med Sci Monit* **18**, CS43–7 (2012).
24. Cannon, R. *et al.* Safety and early efficacy of irreversible electroporation for hepatic tumors in proximity to vital structures. *J Surg Oncol* **107**, 544–9 (2013).
25. Cheung, W. *et al.* Irreversible electroporation for unresectable hepatocellular carcinoma: initial experience and review of safety and outcomes. *Technol Cancer Res Treat* **12**, 233–41 (2013).
26. Tiong, L. & Maddern, G. J. Systematic review and meta-analysis of survival and disease recurrence after radiofrequency ablation for hepatocellular carcinoma. *Br J Surg* **98**, 1210–24 (2011).
27. Golberg, A. & Rubinsky, B. A statistical model for multidimensional irreversible electroporation cell death in tissue. *Bio MedEng OnLine* **9**:13, doi: 10.1186/1475-925X-9-13 (2010).
28. Lee, E. W. *et al.* Advanced hepatic ablation technique for creating complete cell death: irreversible electroporation. *Radiology* **255**, 426–33 (2010).
29. Weaver, J. C. Electroporation of cells and tissues. *IEEE T Plasma Sci* **28**, 24–33 (2000).
30. Weaver, J. C. Electroporation of biological membranes from multicellular to nano scales. *IEEE T Dielectr Electric Insulation* **10**, 754–768 (2003).
31. Sersa, G. *et al.* Vascular disrupting action of electroporation and electrochemotherapy with bleomycin in murine sarcoma. *Br J Cancer* **98**, 388–98 (2008).
32. Grizzi, F. *et al.* Vascular architecture: is it a helpful histopathological biomarker for hepatocellular carcinoma? *J Zhejiang Univ Sci B* **8**, 217–20 (2007).
33. Pavliha, D. *et al.* Electroporation-Based Treatment Planning for Deep-Seated Tumors Based on Automatic Liver Segmentation of MRI Images. *PLoS ONE* **8**, e69068 (2014).
34. Miklavčič, D., Pavšelj, N. & Hart, F. X. [Electric Properties of Tissues] *Wiley Encyclopedia of Biomedical Engineering* (John Wiley & Sons, Inc., 2006).
35. Gessner, U. Effects of the vessel wall on electromagnetic flow measurement. *Biophys J* **1**, 627–37 (1961).

Acknowledgments

We acknowledge Shriners Grant #85120-BOS for the support of this study. We thank Dana-Farber/Harvard Cancer Center in Boston, MA, for the use of the Rodent Histopathology Core, which provided histopathology service. Dana-Farber/Harvard Cancer Center is supported in part by an NCI Cancer Center Support Grant # NIH 5 P30 CA06516.

Author contributions

A.G., B.G.B., B.E.U. and M.Y. designed the study. A.G. and B.G.B. performed the experiments, A.G. developed the FEM model. A.G., B.G.B., B.E.U. and M.Y. drafted, reviewed and approved the manuscript.

Additional information

Competing financial interests: The authors declare no competing financial interests.

How to cite this article: Golberg, A., Bruinsma, B.G., Uygun, B.E. & Yarmush, M.L. Tissue heterogeneity in structure and conductivity contribute to cell survival during irreversible electroporation ablation by “electric field sinks”. *Sci. Rep.* **5**, 8485; DOI:10.1038/srep08485 (2015).



This work is licensed under a Creative Commons Attribution-NonCommercial-ShareAlike 4.0 International License. The images or other third party material in this article are included in the article's Creative Commons license, unless indicated otherwise in the credit line; if the material is not included under the Creative Commons license, users will need to obtain permission from the license holder in order to reproduce the material. To view a copy of this license, visit <http://creativecommons.org/licenses/by-nc-sa/4.0/>